Modelling spreading dynamics of nematic liquid crystals in three spatial dimensions

T.- S. Lin[1],†, L. Kondic[2], U. Thiele[1] and L. J. Cummings[2]

[1]Department of Mathematical Sciences, Loughborough University, Leicestershire LE11 3TU, UK

[2]Department of Mathematical Sciences and Center for Applied Mathematics and Statistics, New Jersey Institute of Technology, Newark, NJ 07102, USA

We study spreading dynamics of nematic liquid crystal droplets within the framework of the long-wave approximation. A fourth-order nonlinear parabolic partial differential equation governing the free surface evolution is derived. The influence of elastic distortion energy and of imposed anchoring variations at the substrate are explored through linear stability analysis and scaling arguments, which yield useful insight and predictions for the behaviour of spreading droplets. This behaviour is captured by fully nonlinear time-dependent simulations of three-dimensional droplets spreading in the presence of anchoring variations that model simple defects in the nematic orientation at the substrate.

Key words: interfacial flows (free surface), liquid crystals, thin films

1. Introduction

Thin liquid films have surprisingly wide application in our daily life. From industrial coating and painting processes to printing, many current technologies require an understanding of fluid flows in which one spatial dimension (the film thickness) is significantly smaller than the others (typically, the lateral scales over which film thickness changes). Under such circumstances one can use systematic asymptotic methods based on a small parameter (the representative aspect ratio of the film, which characterizes the size of the free surface gradients) to simplify the full Navier–Stokes governing equations. Expanding the dependent variables of interest, such as fluid velocity, pressure, etc., in terms of this small parameter, one can obtain a much more tractable system of reduced equations for the leading-order quantities. Despite its simplicity, this approach has been used and experimentally tested many times, and has been very successful in describing the real physics in a wide range of flows.

While plenty of work has been done with Newtonian fluids, this kind of systematic asymptotic treatment of flowing thin complex fluids, in particular liquid crystals, is still in its infancy (see Myers (2005), Blossey *et al.* (2006) and Münch *et al.* (2006) for examples of work on non-Newtonian, but not liquid crystal, thin film flows). Liquid crystals are anisotropic liquids, which typically consist of rod-like molecules. In a nematic phase, the rod-like molecules have no positional order, but they self-align to reach long range directional order. Therefore, to have a complete

† Email address for correspondence: t.lin@lboro.ac.uk

description of a nematic liquid crystal (NLC) flow, one needs to consider not only the velocity field, but also the orientational director field. In experiments on spreading nematic droplets, Poulard & Cazabat (2005) found that NLC droplets spreading on a horizontal substrate exhibit a surprisingly rich range of instabilities, in the regimes where Newtonian droplets would only spread stably (see also Delabre, Richard & Cazabat 2009; Manyuhina, Cazabat & Ben Amar 2010).

With regards to asymptotic (long-wavelength) modelling of such flows, Ben Amar & Cummings (2001) derived a model to describe the surface evolution of strongly anchored, strongly elastic, NLCs, work that was extended by Cummings (2004) to the weakly anchored case; while Carou *et al.* (2007) studied the model for blade coating of NLCs in two-dimensional space in the limit of weak elastic effects. An alternative approach based on energetic arguments was presented by Mechkov, Cazabat & Oshanin (2009). However, these different approaches lead to different predictions for the stability of a thin film; a discrepancy that was reconciled only very recently (Lin *et al.* 2013). We refer the reader to that paper for more details, but briefly, Ben Amar & Cummings (2001) and Cummings (2004) employ the same stress balance at the free surface of the film as in standard Newtonian flow, balancing pressure with capillarity. When this condition is modified to also include an elastic stress, results consistent with the energy-based approach are obtained. Moreover, these consistent results indicate that in the case of strong anchoring conditions at both, the solid substrate and the free surface of the nematic film, such a film is never unstable (Lin *et al.* 2013). Note, that in the weakly elastic limit of Carou *et al.* (2007) the effect does not appear at leading order and no effect on stability is seen. To summarize: many questions remain to be addressed regarding the instability mechanisms in free surface nematic flows. No fully consistent 'lubrication' model for a three-dimensional (3D) situation that can account for the weak anchoring effects that are crucial for instability has yet been proposed or studied.

In this paper, we implement the long-wave approximation to derive a model describing the 3D free surface evolution of a thin film of NLCs on a rigid substrate. The model incorporates a novel weak anchoring surface energy formulation, and shows satisfactory behaviour in the vicinity of a contact line. Simple linear stability analysis (LSA) permits mechanistic insight into how the anchoring energy influences the stability of a spreading NLC droplet.

2. Model derivation

The main dependent variables governing the dynamics of a liquid crystal in the nematic phase are the velocity field $\bar{\boldsymbol{v}} = (\bar{u}, \bar{v}, \bar{w})$, and the director field $\boldsymbol{n} = (n_1, n_2, n_3)$, the unit vector describing the orientation of the anisotropic axis in the liquid crystal (an idealized representation of the local preferred average direction of the rodlike liquid crystal molecules). The director orientation is a function of space and time which, in the limit that director relaxation is fast relative to the flow time scale (the limit considered here) is determined by minimizing a suitably defined total energy. Molecules like to align locally, a preference that is modelled by a bulk elastic (Frank) energy $\bar{W}$, which is minimized subject to boundary conditions. In general, a bounding surface is associated with a given preferred direction for $\boldsymbol{n}$; this preference is known as surface anchoring, and is modelled by an appropriate choice of surface energy. Anchoring can be tuned by appropriate treatment of a surface and may be either weak or strong. The stress tensor for the NLC is a function of the director orientation, hence

elastic effects can strongly influence the fluid flow, giving rise to behaviour that differs markedly from the isotropic Newtonian case.

2.1. *Leslie–Ericksen equations*

The flow of NLCs may be described by the Leslie–Ericksen equations (Leslie 1979). Neglecting inertia, and using over-bars to denote dimensional variables (dimensionless variables will be without bars), the flow is governed by

$$\lambda \boldsymbol{n} - \frac{\partial \bar{W}}{\partial \boldsymbol{n}} + \bar{\boldsymbol{\nabla}} \cdot \left(\frac{\partial \bar{W}}{\partial \bar{\boldsymbol{\nabla}} \boldsymbol{n}} \right) + \bar{\boldsymbol{G}} = 0, \tag{2.1}$$

$$-\bar{\boldsymbol{\nabla}} \cdot \bar{\Pi} + (\bar{\boldsymbol{\nabla}} \boldsymbol{n}) \cdot \bar{\boldsymbol{G}} + \bar{\boldsymbol{\nabla}} \cdot \bar{\boldsymbol{t}} = 0, \tag{2.2}$$

$$\bar{\boldsymbol{\nabla}} \cdot \bar{\boldsymbol{v}} = 0, \tag{2.3}$$

representing energy, momentum and mass conservation, respectively. Here, λ is a Lagrange multiplier ensuring that the director $\boldsymbol{n}$ is a unit vector. The quantities $\bar{W}$, $\bar{\boldsymbol{G}}$ and $\bar{\Pi}$ are defined by

$$2\bar{W} = K[(\bar{\boldsymbol{\nabla}} \cdot \boldsymbol{n})^2 + |\bar{\boldsymbol{\nabla}} \times \boldsymbol{n}|^2], \tag{2.4}$$

$$\bar{G}_i = -\gamma_1 \bar{N}_i - \gamma_2 \bar{e}_{ik} n_k, \quad \bar{e}_{ij} = \frac{1}{2} \left(\frac{\partial \bar{v}_i}{\partial \bar{x}_j} + \frac{\partial \bar{v}_j}{\partial \bar{x}_i} \right), \tag{2.5}$$

$$\bar{N}_i = \dot{n}_i - \bar{\omega}_{ik} n_k, \quad \bar{\omega}_{ij} = \frac{1}{2} \left(\frac{\partial \bar{v}_i}{\partial \bar{x}_j} - \frac{\partial \bar{v}_j}{\partial \bar{x}_i} \right), \tag{2.6}$$

$$\bar{\Pi} = \bar{p} + \bar{W} + \bar{\psi}_g, \tag{2.7}$$

where K is an elastic constant (this form of $\bar{W}$ (2.12) exploits the widely used one-constant approximation (De Gennes & Prost 1995)), γ_1 and γ_2 are constant viscosities; an over-dot denotes a material (total) time derivative, subscripts i, j and k denote vector indices and the Einstein summation convention is used; $\bar{p}$ is the pressure and $\bar{\psi}_g$ is the gravitational potential. Finally, $\bar{\boldsymbol{t}}$ is the viscous stress tensor with components

$$\bar{t}_{ij} = \alpha_1 n_k n_p \bar{e}_{kp} n_i n_j + \alpha_2 \bar{N}_i n_j + \alpha_3 \bar{N}_j n_i + \alpha_4 \bar{e}_{ij} + \alpha_5 \bar{e}_{ik} n_k n_j + \alpha_6 \bar{e}_{jk} n_k n_i, \tag{2.8}$$

where α_i are constant viscosities (related to γ_i in (2.5) by $\gamma_1 = \alpha_3 - \alpha_2$, $\gamma_2 = \alpha_6 - \alpha_5$, and to each other by the Onsager relation, $\alpha_2 + \alpha_3 = \alpha_6 - \alpha_5$).

2.2. *Non-dimensionalization*

We employ long-wave scalings to non-dimensionalize the governing equations

$$(\bar{x}, \bar{y}, \bar{z}) = (Lx, Ly, \delta Lz), \quad (\bar{u}, \bar{v}, \bar{w}) = (Uu, Uv, \delta Uw), \tag{2.9}$$

$$\bar{t} = \frac{L}{U} t, \quad \bar{p} = \frac{\mu U}{\delta^2 L} p, \quad \bar{W} = \frac{K}{\delta^2 L^2} W, \tag{2.10}$$

where L is the length scale of typical variations parallel to the substrate, U is the typical flow speed, $\delta = h_0/L \ll 1$ is the aspect ratio of typical variations of the film height h_0 (a small slope assumption) and $\mu = \alpha_4/2$ is chosen as the representative viscosity scaling in the pressure, since this corresponds to the usual viscosity in the isotropic case. Our choices of L and U are discussed later in the text.

2.3. *Energetics of director field*

It has been shown (Ben Amar & Cummings 2001; Cummings 2004) that with the above scalings, and provided the inverse Ericksen number $K/(\mu UL) = O(1)$,

the coupling terms in (2.1)–(2.3) between the energy and momentum equations, represented by $\bar{G}$, can be neglected. The energy equations then reduce to the appropriate Euler–Lagrange equations for minimizing the free energy of the film subject to the constraint $\boldsymbol{n}\cdot\boldsymbol{n} = 1$, corresponding to the limit of instantaneous relaxation of the director field. Imposing the constraint $\boldsymbol{n}\cdot\boldsymbol{n} = 1$ directly we have a director field that is a vector on the unit sphere characterized by two angles,

$$\boldsymbol{n} = (\sin\theta\cos\phi, \sin\theta\sin\phi, \cos\theta), \qquad (2.11)$$

for some functions $\theta(x, y, z, t)$ and $\phi(x, y, z, t)$, which are the usual spherical polar angles.

The leading-order bulk elastic energy, under the long-wave scaling, is given by

$$2W = \theta_z^2 + \phi_z^2\sin^2\theta + O(\delta). \qquad (2.12)$$

The surface energy at the free surface $z = h(x, y, t)$ is denoted by $\mathscr{G} = \mathscr{G}(\hat{\theta})$ where $\hat{\theta}$ is the conical director orientation at the free surface,

$$\hat{\theta} = \theta(x, y, h, t). \qquad (2.13)$$

The surface energy $\mathscr{G}$ takes its minimum when the director takes the preferred orientation $\hat{\theta} = 0$. Within the long-wave approximation this corresponds to a director field perpendicular to the free surface: *homeotropic* surface anchoring. At the substrate $z = 0$ we assume strong *planar* anchoring, $\theta(x, y, 0, t) = \pi/2$, with ϕ specified. These anchoring assumptions are consistent with the experiments of Poulard & Cazabat (2005) (but not to all experimental spreading scenarios; in particular our model is not applicable to the case of fully degenerate planar anchoring at the lower substrate).

We carry out the free energy minimization directly using a variational principle. The total free energy, J, consists of bulk and surface contributions. We write

$$J = \int_0^h \int_\Omega \tilde{\mathscr{N}} W \, \mathrm{d}S \, \mathrm{d}z + \int_\Omega \mathscr{G} \, \mathrm{d}S, \qquad (2.14)$$

where Ω is the domain occupied by the liquid crystal sample in the x–y plane and $\tilde{\mathscr{N}} = K/(\mu UL)$ is the inverse Ericksen number. We consider the variations induced in J by small variations in the fields θ and ϕ. The first variations must both vanish at an extremum and the sign of the second variations tells us whether or not we have an energy minimum. After an integration by parts, the vanishing of the bulk terms in the first variations of J leads to

$$\theta_{zz} = \frac{\phi_z^2}{2}\sin 2\theta \quad \text{in } \Omega \cup \{0 < z < h\}, \qquad (2.15)$$

$$(\phi_z\sin^2\theta)_z = 0 \quad \text{in } \Omega \cup \{0 < z < h\}. \qquad (2.16)$$

At the free surface, the surface energy $\mathscr{G}$ is independent of the azimuthal angle ϕ (conical anchoring), hence a natural boundary condition on ϕ emerges from the surface contribution to the first variation of J with respect to ϕ: $\phi_z\sin^2\theta = 0$ on $z = h$. The angle ϕ is thus independent of z; and with our assumption of strong anchoring at the substrate, we then have

$$\phi = \phi(x, y) \qquad (2.17)$$

determined by the imposed substrate anchoring pattern. For θ, (2.15) reduces to $\theta_{zz} = 0$, and the strong planar anchoring condition is imposed on $z = 0$. We then have

$$\theta = a(x, y, t)z + \frac{\pi}{2}, \tag{2.18}$$

where a is determined by the condition that the surface contribution in the first variation vanish,

$$\frac{\mathrm{d}\mathscr{G}}{\mathrm{d}\hat{\theta}} + \tilde{\mathscr{N}} a = 0. \tag{2.19}$$

2.3.1. *Surface energy*

For relatively thick films, the director angle θ can easily adjust to the preferred values at each surface. As the film gets thin, and in particular near precursor layers or contact lines, there is a very large energy penalty to pay for bending between two fixed angles across a very short distance h. In this paper we assume the existence of a thin precursor film ahead of a bulk droplet, of thickness $0 < b \ll 1$ (this is also the case in the experiments of Poulard & Cazabat (2005)). To avoid a near-singularity in the director orientation within the precursor, we allow the anchoring to be relaxed as $h \to b$.

To capture these two limiting behaviours for thick and very thin films, we propose that the change in director angle across the fluid layer, ah, approaches a prescribed value Θ (the difference in the preferred angles at the free surface and solid substrate) as $h \to \infty$; and approaches zero as the film thickness $h \to b$. Similar to the approach of Cummings, Lin & Kondic (2011), we introduce an *ad hoc* anchoring condition based on specifying this change in director angle by

$$ah = \Theta m(h), \tag{2.20}$$

where $m(h)$ is a monotone increasing function of h with $m(b) = 0$ and $m(\infty) = 1$. With our assumption of homeotropic alignment at the free surface (and with the assumed lubrication scalings), $\Theta = -\pi/2$.

Although we have not yet explicitly given the surface energy $\mathscr{G}$, it is implicitly imposed and easily recovered. Based on the above, the director angle θ is given by $\theta = (\pi/2)(1 - zm(h)/h)$, so that the angle $\hat{\theta}$ at the free surface, defined by (2.13), is given as a function of h by

$$\hat{\theta} = \frac{\pi}{2}(1 - m(h)). \tag{2.21}$$

The surface energy must satisfy (2.19). Since (2.21) is not trivially inverted to give $h(\hat{\theta})$, we use the chain rule to obtain

$$\frac{\mathrm{d}\mathscr{G}}{\mathrm{d}h} = \frac{\mathrm{d}\mathscr{G}}{\mathrm{d}\hat{\theta}}\frac{\mathrm{d}\hat{\theta}}{\mathrm{d}h} = -\mathscr{N}\frac{m(h)m'(h)}{h}, \tag{2.22}$$

where $\mathscr{N} = \Theta^2\tilde{\mathscr{N}}$. Equation (2.22) defines the surface energy $\mathscr{G}$ in terms of the film height h. The expression in terms of director angle at the free surface, $\hat{\theta}$, may be recovered by use of (2.21).

Note that (2.18) and (2.20) also imply that the bulk elastic energy in (2.12) becomes

$$W = \frac{\Theta^2}{2}\frac{m^2}{h^2}. \tag{2.23}$$

As a result we have the contribution of nematic elasticity to the free energy as

$$J = \int_{\Omega} \left[\frac{\mathcal{N}}{2} \frac{m^2}{h} + \mathcal{G} \right] dS. \tag{2.24}$$

2.4. *Momentum equation*

For the momentum equations (2.2), balancing dominant terms gives

$$\frac{\partial \Pi}{\partial x} \sim \frac{\partial t_{13}}{\partial z}, \quad \frac{\partial \Pi}{\partial y} \sim \frac{\partial t_{23}}{\partial z},$$

in dimensionless form. Based on the long-wave scalings, to leading order we have

$$t_{13} = (A_1 + A_2 \cos 2\phi)u_z + A_2 \sin 2\phi v_z, \quad t_{23} = A_2 \sin 2\phi u_z + (A_1 - A_2 \cos 2\phi)v_z, \tag{2.25}$$

where $A_1 = 1 + (\alpha_5 - \alpha_2)\cos^2\theta + \alpha_1 \sin^2\theta \cos^2\theta + ((\alpha_3 + \alpha_6)/2)\sin^2\theta$, $A_2 = \alpha_1 \sin^2\theta \cos^2\theta + ((\alpha_3 + \alpha_6)/2)\sin^2\theta$, and the α_i are normalized by $\mu = \alpha_4/2$. As a result, the leading-order equations are

$$\frac{\partial p}{\partial x} + \tilde{\mathcal{N}} \theta_z \theta_{zx} = \frac{\partial}{\partial z} \left\{ (A_1 + A_2 \cos 2\phi)u_z + A_2 \sin 2\phi v_z \right\}, \tag{2.26}$$

$$\frac{\partial p}{\partial y} + \tilde{\mathcal{N}} \theta_z \theta_{zy} = \frac{\partial}{\partial z} \left\{ A_2 \sin 2\phi u_z + (A_1 - A_2 \cos 2\phi)v_z \right\}, \tag{2.27}$$

$$\frac{\partial p}{\partial z} = -\mathcal{B}, \tag{2.28}$$

where $\mathcal{B} = \delta^3 \rho g L^2 / \mu U$ is the Bond number.

We assume that the normal component of the stress at the free surface balances surface tension (the isotropic component of the surface energy, γ) times curvature, and that the in-plane component of the stress is balanced by surface tension (surface energy) gradients in the plane of the surface. This yields the leading-order boundary conditions:

$$p + \tilde{\mathcal{N}} \theta_z^2 = -\mathcal{C} \nabla^2 h, \tag{2.29}$$

$$-\tilde{\mathcal{N}} (\theta_x \theta_z + \theta_z^2 h_x) + (A_1 + A_2 \cos 2\phi)u_z + A_2 \sin 2\phi v_z = \tilde{\mathcal{N}} \mathcal{G}_x, \tag{2.30}$$

$$-\tilde{\mathcal{N}} (\theta_y \theta_z + \theta_z^2 h_y) + A_2 \sin 2\phi u_z + (A_1 - A_2 \cos 2\phi)v_z = \tilde{\mathcal{N}} \mathcal{G}_y, \tag{2.31}$$

where $\mathcal{C} = \delta^3 \gamma / \mu U$ is an inverse capillary number. Furthermore, using (2.19)–(2.21), the equations of the tangential stress balances (2.30)–(2.31) reduce to $u_z = 0$ and $v_z = 0$.

We solve (2.28)–(2.29) for p

$$p = \mathcal{B}(h - z) - \tilde{\mathcal{N}} a^2 - \mathcal{C} \nabla^2 h, \tag{2.32}$$

and substitute in (2.26)–(2.27) to obtain u_z and v_z using the boundary conditions derived above:

$$D u_z = [(A_1 - A_2 \cos 2\phi)(p_x + \tilde{\mathcal{N}} a a_x) - A_2 \sin 2\phi (p_y + \tilde{\mathcal{N}} a a_y)](z - h), \tag{2.33}$$

$$D v_z = [(A_1 + A_2 \cos 2\phi)(p_y + \tilde{\mathcal{N}} a a_y) - A_2 \sin 2\phi (p_x + \tilde{\mathcal{N}} a a_x)](z - h), \tag{2.34}$$

where $D = A_1^2 - A_2^2$. Finally, using conservation of mass together with the relations

$$\int_0^h u\,\mathrm{d}z = \int_0^h u_z(h-z)\,\mathrm{d}z, \qquad \int_0^h v\,\mathrm{d}z = \int_0^h v_z(h-z)\,\mathrm{d}z, \qquad (2.35)$$

we obtain a partial differential equation (PDE) governing the evolution of the film height:

$$h_t + \nabla \cdot \left[\left\{ \mathfrak{f}_1 \boldsymbol{I} + \mathfrak{f}_2 \begin{bmatrix} \cos 2\phi & \sin 2\phi \\ \sin 2\phi & -\cos 2\phi \end{bmatrix} \right\} \cdot \nabla \left(\mathscr{C}\nabla^2 h - \mathscr{B}h + \frac{\tilde{\mathscr{N}}}{2}a^2 \right) \right] = 0, \quad (2.36)$$

where $\boldsymbol{I}$ is the identity matrix and

$$\mathfrak{f}_1 = \int_0^h \frac{A_1}{A_1^2 - A_2^2}(h-z)^2\,\mathrm{d}z, \quad \mathfrak{f}_2 = \int_0^h \frac{-A_2}{A_1^2 - A_2^2}(h-z)^2\,\mathrm{d}z. \qquad (2.37)$$

Equations (2.36)–(2.37) represent a formidable analytical challenge. We simplify by approximating the integral expressions using the two-point trapezoidal rule, as

$$\mathfrak{f}_1 = \lambda h^3, \quad \mathfrak{f}_2 = \nu h^3, \quad \lambda = \frac{2 + \alpha_3 + \alpha_6}{4(1 + \alpha_3 + \alpha_6)}, \quad \nu = -\frac{\alpha_3 + \alpha_6}{4(1 + \alpha_3 + \alpha_6)}. \qquad (2.38)$$

For $-1 < \alpha_3 + \alpha_6 < 0$ (which is the case for all common NLCs), we have $\lambda > \nu > 0$. By including these quantities and our chosen surface energy $\mathscr{G}$ from §2.3.1, the equation can be rewritten as

$$h_t + \nabla \cdot \left[h^3 \tilde{\nabla} \left(\mathscr{C}\nabla^2 h - \mathscr{B}h \right) + \mathscr{N} \left(mm'h - m^2 \right) \tilde{\nabla} h \right] = 0, \qquad (2.39)$$

where $\mathscr{N} = \Theta^2 K / \mu U L$ and

$$\tilde{\nabla} = \left(\lambda \boldsymbol{I} + \nu \begin{bmatrix} \cos 2\phi & \sin 2\phi \\ \sin 2\phi & -\cos 2\phi \end{bmatrix} \right) \cdot \nabla. \qquad (2.40)$$

2.5. *Model summary*

Our final model consists of the PDE (2.39), where $\tilde{\nabla}$ is defined in (2.40), with the anchoring condition at the free surface, $m(h)$, and the anchoring pattern at the substrate, $\phi(x, y)$, to be specified. We have five dimensionless positive parameters, λ, ν, $\mathscr{C}$, $\mathscr{B}$ and $\mathscr{N}$, giving a solution space that is potentially very large. In the following analysis and simulations, we assume a balance between surface tension and gravity, setting $\mathscr{C} = \mathscr{B} = 1$, meaning physically that the typical length scale L considered is the capillary length, $\sqrt{\gamma/\rho g}$. Clearly, alternative choices can be made if a different balance, or different length scales, are to be considered.

On the other hand, it has been shown (Lin *et al.* 2013) that the evolution equation for a NLC film in the limit of strong anchoring can be written in a variational or gradient dynamics form in line with such formulations for films of simple liquids (see, e.g., Mitlin 1993; Thiele 2010), films of mixtures (Thiele 2011) and surfactant-covered films (Thiele, Archer & Plapp 2012). We would like to point out that this is also true for the current model. In such a formulation, the evolution of the film thickness h follows a dissipative gradient dynamics governed by the equation

$$h_t = \nabla \cdot \left[Q(h) \tilde{\nabla} \left(\frac{\delta F}{\delta h} \right) \right], \qquad (2.41)$$

where $Q(h)$ is the mobility function and F is the free energy functional written as

$$F[h] = \int_\Omega \left[\mathscr{C} \left(1 + \frac{(\nabla h)^2}{2} \right) + \frac{\mathscr{B}}{2} h^2 \right] dS + J. \tag{2.42}$$

The contribution of nematic elasticity to the free energy functional, J, is given in (2.24). By introducing F into (2.41) and noting that the surface energy $\mathscr{G}$ is coupled with the film thickness through (2.22), we obtain the evolution equation

$$h_t = \nabla \cdot \left[Q(h) \tilde{\nabla} \left(-\mathscr{C} \nabla^2 h + \mathscr{B} h - \frac{\mathscr{N}}{2} \frac{m^2}{h^2} \right) \right]. \tag{2.43}$$

One should note that (2.39) and (2.43) are identical when $Q(h) = h^3$.

3. Analysis and results

In this section we investigate some limiting cases of the model analytically, and carry out additional simulations for spreading nematic films and droplets in selected flow configurations. The time-dependent simulations that we report below are based on an alternative-direction-implicit (ADI) method (as outlined by Witelski & Bowen (2003)) with variable time stepping based on a Crank–Nicolson scheme; see Lin, Kondic & Filippov (2012*b*) for further details.

3.1. *Influence of anchoring patterns at the substrate*

To gain some insight into our model we first compare two different unidirectional substrate anchoring patterns, in the simple case where flow is independent of y, and the fluid spreads uniformly in the x direction. Assuming $\phi = 0$ (director orientation at the substrate parallel to the fluid flow direction), equation (2.39) becomes

$$h_t + (\lambda + \nu) \partial_x \left[h^3 (h_{xxx} - h_x) + \mathscr{N} \left(mm'h - m^2 \right) h_x \right] = 0. \tag{3.1}$$

If, on the other hand, we assume $\phi = \pi/2$, so that the substrate director orientation is perpendicular to the fluid flow (but still in the plane of the substrate), equation (2.39) becomes

$$h_t + (\lambda - \nu) \partial_x \left[h^3 (h_{xxx} - h_x) + \mathscr{N} \left(mm'h - m^2 \right) h_x \right] = 0. \tag{3.2}$$

Equations (3.1) and (3.2) are identical once time is rescaled by a constant. In this simple example, the substrate pattern only affects the flow time scale, effectively making the fluid viscosity ϕ-dependent. The NLC flows faster when the anchoring pattern is parallel to the flow direction (effective viscosity is smaller), and slower when it is perpendicular (effective viscosity is larger).

To focus more on the influence of the anchoring patterns at the substrate, we next consider a weak conical free surface anchoring on θ so that the director orientation is mainly determined by the strong planar anchoring at the substrate, i.e. $\theta \equiv \pi/2$ and $m(h) \equiv 0$. The contribution of nematic bending elasticity then disappears. In particular, the integral expressions in (2.37) can now be evaluated exactly; there is no need to approximate them as was done to obtain (2.39). The resulting equation is

$$h_t + \nabla \cdot \left[\frac{2h^3}{3} \tilde{\nabla} \left(\nabla^2 h - h \right) \right] = 0. \tag{3.3}$$

Figure 1 shows the solution of (3.3) computed using ADI-based simulations of a configuration where the anchoring imposed at the substrate appears as a striped pattern,
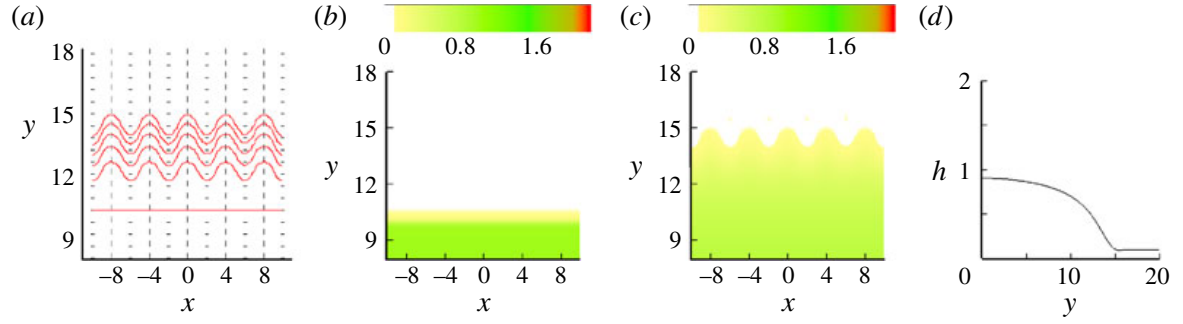
FIGURE 1. (Colour online) Spreading NLC film on a stripe-patterned substrate ($\lambda = 1$, $\nu = 0.5$, $\mathcal{N} = 0$). (*a*) The dashed (black) lines indicate the anchoring at the substrate. The solid (shown in red online) curves show the front position at $\Delta t = 10$ time intervals between successive curves. The initial front position is shown as a straight (shown in red online) line at $y \approx 10$. (*b–c*) Surface contour plot of the film at $t = 0, 50$, respectively. (*d*) Cross-section of the film, $h(x = 0, y, t = 50)$.

as shown in figure 1(*a*): $\phi = \pi/2$ for $x \in (4n - 1, 4n + 1)$, $n = 0, \pm 1$ and ± 2; and $\phi = 0$ otherwise. The initial film profile, shown as a surface contour plot in figure 1(*b*), is taken as

$$h(x, y, 0) = 0.45 \tanh(-5(y - 10)) + 0.55, \tag{3.4}$$

with the front position being a straight line parallel to the x-axis, and spreading in the $+y$ direction. The computational domain is defined by $-L_x \leqslant x \leqslant L_x$ and $0 \leqslant y \leqslant L_y$, with $L_x = 10$ and $L_y = 20$. The implemented boundary conditions are $h_x(\pm L_x, y, t) = h_y(x, 0, t) = h_y(x, L_y, t) = h_{xxx}(\pm L_x, y, t) = h_{yyy}(x, 0, t) = 0$, $h(x, L_y, t) = b$, where b is the thickness of the prewetting layer (precursor film) used to remove the contact line singularity. In the simulation scenarios that follow (in both this and the following section), the exact value given to b was found to have only a weak influence on spreading (with faster spreading for larger b), but no influence of the exact value of b on the stability of the flow has been found. We use $b = 0.1$ here, and on uniform computational grids specified by the grid spacing $\delta x = \delta y = 0.1$; these values are found to be sufficient to guarantee numerical convergence.

Figure 1(*a*) shows the evolution of the spreading fluid front. The anchoring pattern at the substrate clearly influences the spreading: as figure 1(*a*) shows, in line with the observations discussed above, the front moves fastest when the fluid motion is parallel to the anchoring pattern, and slowest when flow is perpendicular to anchoring. As the anchoring changes periodically, the speed of the front transitions between the two extremes, giving rise to a sawtooth pattern. It should be noted that although (3.1) and (3.2) are indicative of different wavespeeds for an isolated moving front, the amplitude of the front perturbation does not increase linearly in time, as seen in figure 1(*a*). Instead, the amplitude approaches a constant value. This constant amplitude is determined by the balance between different effective viscosities and surface tension effects.

Figure 1(*c*) shows a surface contour plot of the profile at a late time, $t = 50$, and figure 1(*d*) shows its cross-section at $x = 0$. Note the absence of a capillary ridge behind the front, indicating the stability of the underlying flow. The sawtooth pattern that develops in the spreading front here, although reminiscent of a fingering instability, is no such thing: it is simply the result of the anchoring inhomogeneity imposed at the substrate.

3.2. *Influence of anchoring condition at the free surface*

We now analyse the effect of free surface anchoring on the director angle, θ. We begin by reviewing the LSA of a simple flat film of height $h = h_0$ in the two-dimensional case in which variations with respect to the y coordinate are neglected, so that both director field and flow are confined to the (x, z)-plane (Cummings *et al.* 2011). This analysis is found in practice to give a remarkably good indication regarding stability of spreading 3D droplets, considered in § 3.3 below. In that section we present several simulations of stable/unstable 3D droplet evolution of a chosen surface anchoring function to illustrate the kind of behaviour that our model can reproduce in the presence of some simple substrate anchoring patterns.

3.2.1. *LSA of a flat film*

With the director confined to the (x, z) plane, $\phi \equiv 0$, and no y-dependence, equation (2.39) reduces to (3.1). Assuming $h = h_0 + \xi$ and $|\xi| \ll h_0$ in this equation, we find

$$\xi_t + (\lambda + \nu)h_0^3 \left[\xi_{xxxx} - \xi_{xx} + \mathcal{N}M(h_0)\xi_{xx}\right] = 0, \tag{3.5}$$

where

$$M(h) = \frac{m(h)m'(h)h - m(h)^2}{h^3}. \tag{3.6}$$

By setting $\xi \propto \exp(\mathrm{i}kx + \omega t)$, we obtain the dispersion relation

$$\omega = -(\lambda + \nu)h_0^3 \left[k^4 + (1 - \mathcal{N}M(h_0))k^2\right]. \tag{3.7}$$

The flat film is thus unstable to sufficiently long-wavelength perturbations if $\mathcal{N}M(h_0) > 1$. When this is the case, perturbations with wavenumbers $k \in (0, k_c)$ are unstable, where $k_c = \sqrt{\mathcal{N}M(h_0) - 1}$ is the critical wavenumber. The fastest-growing wavenumber (for which the growth rate is the largest) is $k_m = k_c/\sqrt{2}$, corresponding to the wavelength

$$l_m = \frac{2\pi}{k_m} = \frac{2\pi}{\sqrt{(\mathcal{N}M(h_0) - 1)/2}}, \tag{3.8}$$

and the growth rate $\omega_m = (\lambda + \nu)h_0^3(\mathcal{N}M(h_0) - 1)^2/4$.

3.2.2. *Strong surface anchoring*

We consider firstly a strong homeotropic anchoring, given by $m \equiv 1$. In this limit, the evolution equation becomes

$$h_t + \nabla \cdot \left[h^3\tilde{\nabla}\left(\mathscr{C}\nabla^2 h - \mathscr{B}h\right) - \mathcal{N}\tilde{\nabla}h\right] = 0, \tag{3.9}$$

Note that, the elastic contributions to the governing equation are purely diffusive. A version of this limit was derived via alternative energetic considerations by Mechkov *et al.* (2009) (see also Lin *et al.* (2013) for a more in-depth discussion of the strong anchoring case). Although the director field corresponding to strong anchoring becomes singular as the film height $h \to 0$, the PDE governing the film height in this limit is well-behaved and will never exhibit an instability. This observation suggests that the weak free surface anchoring, necessary on physical grounds for the director to be non-singular as the film height goes to zero, is key for the instability mechanism.
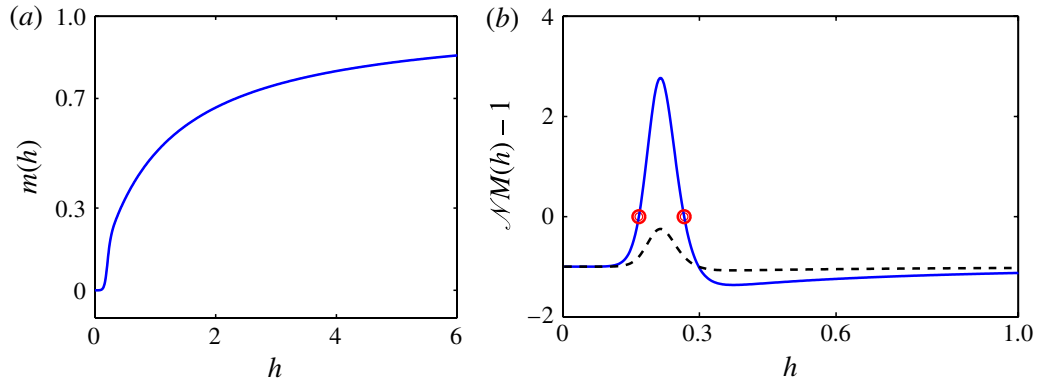
FIGURE 2. (Colour online) (*a*) The anchoring condition, $m(h)$, as defined in (3.10) with $\alpha = \beta = 1$ and $b = 0.1$, $w = 0.05$. (*b*) $\mathcal{N}M(h) - 1$ as a function of h where $M(h)$ is defined in (3.6). The solid (shown in blue online) curve is for $\mathcal{N} = 1$ and the dashed (black) curve for $\mathcal{N} = 0.2$. The circles (shown in red online) indicate the critical values where $\mathcal{N}M(h) - 1 = 0$.

3.2.3. *Weak surface anchoring*

For a weak surface anchoring, there are many possible forms for $m(h)$ that satisfy our basic requirement $m(b) = 0$, $m(\infty) = 1$. Here, as an example, we take

$$m(h) = f(h; b)\left(\frac{h^{\alpha}}{h^{\alpha} + \beta^{\alpha}}\right) \tag{3.10}$$

where α and β are positive constants that tune the relaxation of the anchoring for film heights larger than the precursor, and $f(h; b)$ provides the 'cutoff' behaviour as the precursor is approached. In the simulations presented in this paper we choose $f(h; b) = [\tanh((h - 2b)/w) + 1]/2$, where w fixes the size of the h-range over which $m(h)$ is turned off as $h \to b$ ($w \to 0$ gives a simple discontinuous switch; we assign a small positive value, $w = 0.05$, to smooth this behaviour). This choice for $m(h)$ ensures that the director field for thin films, roughly less than b, lies in the plane $\theta = \pi/2$, with ϕ dictated by the substrate anchoring conditions. We note that the exact functional form given to $m(h)$ does not influence the results to any significant degree, as long as $m(h)$ changes sufficiently rapidly for $h \sim b$.

Figure 2(*a*) shows the anchoring condition at the free surface, (3.10), with $\alpha = \beta = 1$ and $b = 0.1$. It can be seen that the anchoring condition approaches 0 for thin films and increasingly approaches 1 when the film thickness gets thicker. Figure 2(*b*) shows the function $\mathcal{N}m(h) - 1$ for $\mathcal{N} = 0.2$ (dashed (black) curve) and for $\mathcal{N} = 1$ (solid (shown in blue) curve). As demonstrated in § 3.2.1, (3.7), the flat film with thickness h_0 is unstable if $\mathcal{N}m(h_0) - 1 > 0$. One can see that for $\mathcal{N} = 0.2$, flat films are always stable while for $\mathcal{N} = 1$, there exists a range of film thicknesses (the critical values are marked by circles (shown in red online) in figure 2*b*) that exhibit instabilities.

3.3. *Numerical results*

In this section we present several simulations of 3D spreading nematic droplets, in which the influence of the anchoring condition at the substrate can be directly investigated. In particular, as test cases we consider spreading on substrate anchoring patterns that mimic the director structure near different types of nematic defects, in order to analyse the influence of local director structure on spreading (see Lin, Kondic & Cummings (2012*a*) for a related analysis of strictly two-dimensional 'defects'). Such defects are classified according to their topological winding number *s*: as a small
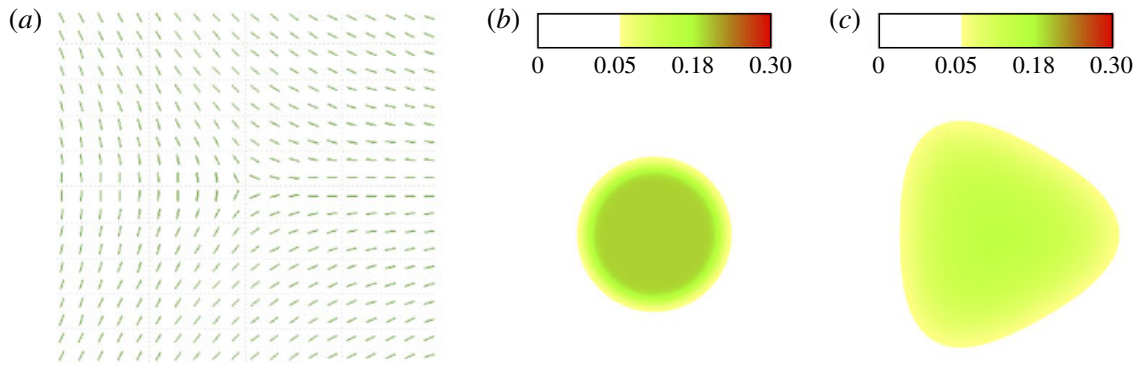
FIGURE 3. (Colour online) Spreading NLC droplet for $\mathcal{N} = 0.2$ and $s = -1/2$. (*a*) The anchoring condition at the substrate, $\phi(x, y)$, as defined in (3.11). (*b*) The initial condition at $t = 0$. (*c*) The droplet evolution at $t = 10\,000$.

planar circuit around the defect is traversed exactly once, the director field rotates through an angle $2\pi s$. Specifically, we have

$$\phi(x, y) = s \tan^{-1}\left(\frac{y}{x}\right). \tag{3.11}$$

While this description cannot capture the true physics very close to the defect centre (the director field notion breaks down there and one has to introduce a tensorial order parameter for a detailed description; see e.g. De Gennes & Prost (1995) for a discussion) we suggest that it may provide a reasonable description of the macroscopic free surface evolution in the presence of a pinned defect. More importantly, for different choices of s, equation (3.11) provides examples of generic surface anchoring patterns that provide useful demonstrations of our model behaviour.

We solve numerically (2.39) on such an anchoring pattern, our choice of parameters is guided by the LSA results presented in § 3.2.1 above. The computational domain in all cases is chosen as $-L_x \leqslant x \leqslant L_x$ and $-L_y \leqslant y \leqslant L_y$ with $L_x = L_y = 20$, and with the boundary conditions

$$h(x, \pm L_y, t) = h(\pm L_x, y, t) = b, \quad h_y(x, \pm L_y, t) = h_x(\pm L_x, y, t) = 0. \tag{3.12}$$

For our first set of simulations we take as initial condition a smoothed cylinder of radius 10 and height $h_0 = 0.2$, with a precursor film of thickness $b = 0.05$ covering the rest of the domain. While the exact functional form for $h(x, y, 0)$ only weakly influences the subsequent evolution, we give it here for definiteness:

$$h(x, y, 0) = \frac{h_0 - b}{2} \tanh\left(-\left(\sqrt{x^2 + y^2} - 10\right)\right) + \frac{h_0 + b}{2}. \tag{3.13}$$

Finally, the parameters appearing in (2.40), (3.10) are chosen as $\alpha = 1$, $\beta = 1$, $\lambda = 1$ and $\nu = 1/2$. The value of $\mathcal{N}$ is given in each figure caption.

Figure 3(*b,c*) shows the evolution of a stably spreading nematic droplet, for $\mathcal{N} = 0.2$. The anchoring at the substrate mimics the director structure near a defect of type $s = -1/2$, shown in figure 3(*a*). Owing to the non-uniformity of this pattern in the radial direction, the droplet spreads asymmetrically, but in the manner that might be expected for the prescribed anchoring pattern. Consistent with the results of our LSA in § 3.2.1 we do not observe any free surface instabilities: the corresponding flat film is stable for the chosen parameters.
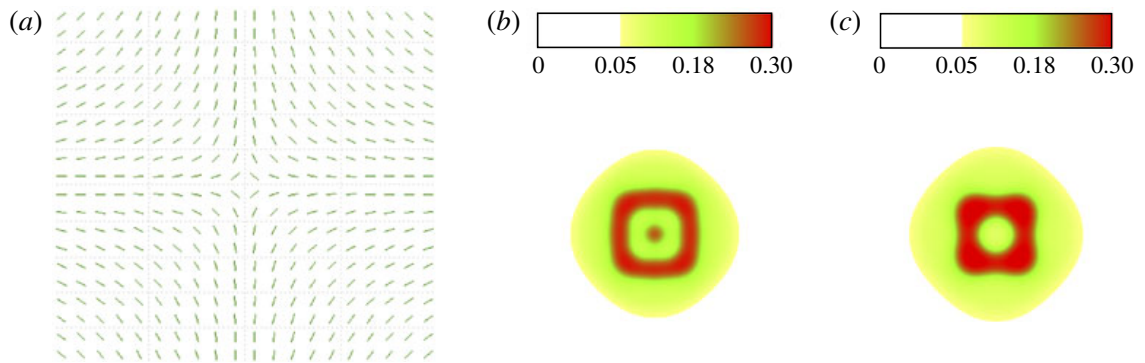
FIGURE 4. (Colour online) Spreading NLC droplet for $\mathcal{N} = 1$ and $s = -1$. The initial condition is the same as in figure 3(*b*). The anchoring condition at the substrate is shown in (*a*). The droplet evolution at $t = 500$ and $t = 1000$ are shown in (*b*,*c*), respectively.

Figure 4 shows the evolution of a spreading nematic droplet, for $\mathcal{N} = 1$. The anchoring at the substrate mimics the four-fold symmetric director structure near a defect of type $s = -1$, shown in figure 4(*a*). Again, due to the non-uniformity of this pattern in the radial direction, the droplet spreads in the manner that might be expected for the prescribed anchoring pattern. In addition, we observe rich pattern formation on the droplet surface, as illustrated by figure 4(*b*–*c*).

By the analysis of § 3.2.1, a flat film of the same thickness $h_0 = 0.2$ is unstable for $\mathcal{N} = 1$. The most unstable wavelength for this case is $l_m \approx 2\pi$, predicting that there will be ∼3 humps on the droplet surface for the chosen initial condition. We find that the results of simulations are consistent with these predictions, see, e.g. figure 4(*b*). The cross-section in the radial direction of this figure shows three hump-like structures, specified by (in three dimensions) one raised ring with one spherical hump at the centre.

In order to confirm that this comparison between the LSA and nonlinear simulations extends to other parameter values, we next consider $\mathcal{N} = 10$. Here, the LSA predicts that the most unstable wavelength is $l_m \approx 1.6$ and the number of humps for the drop considered should be ∼12. Figure 5 shows this case, for a droplet spreading on an anchoring pattern given by (3.11) with $s = 1/2$. We again find remarkably good agreement between the LSA prediction for the flat film, and the observed simulation for the cylindrical droplet. Figure 5(*b*), for example, shows that there are 6 rings that form, corresponding in the cross-section to 12 humps. Also note that the time scale for instability development is much shorter for $\mathcal{N} = 10$. Here, the unstable pattern has developed already at $t = 5$, see figure 5(*b*), while for $\mathcal{N} = 1$ we have to wait until $t = 500$, as shown in figure 4(*b*). This finding is also consistent with the LSA predictions. We remark also that the type of structures seen in figure 5(*c*) are reminiscent of certain free surface structures seen in the experiments of Poulard & Cazabat (2005) (albeit within a much more complicated setting in those experiments).

Finally, in figure 6 we show a spreading NLC droplet on a radially symmetric anchoring pattern, which mimics the director structure near a defect of type $s = 1$. The parameter $\mathcal{N}$ is set to unity. Instead of using a cylindrical cap as the initial condition, here we choose one that is closer to a spherical cap, shown as the solid (black) curve in figure 6(*b*), a configuration for which our LSA is not applicable. Nonetheless we note that, taking h_0 in the LSA to be the mean initial droplet height, one might anticipate instability for these parameter values. As the droplet spreads, the front
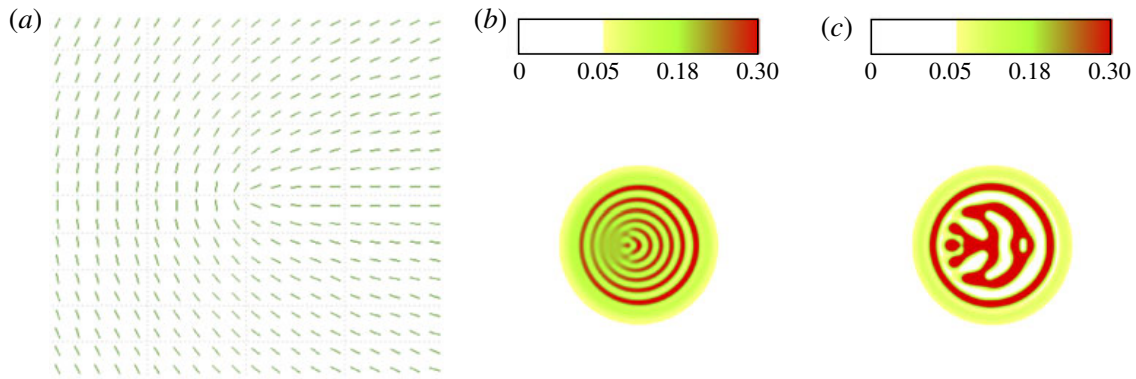
FIGURE 5. (Colour online) Spreading NLC droplet for $\mathcal{N} = 10$ and $s = 1/2$. The initial condition is the same as in figure 3(b). The anchoring condition at the substrate is shown in (a). The droplet evolution at $t = 5$ and 30 is shown in (b,c).
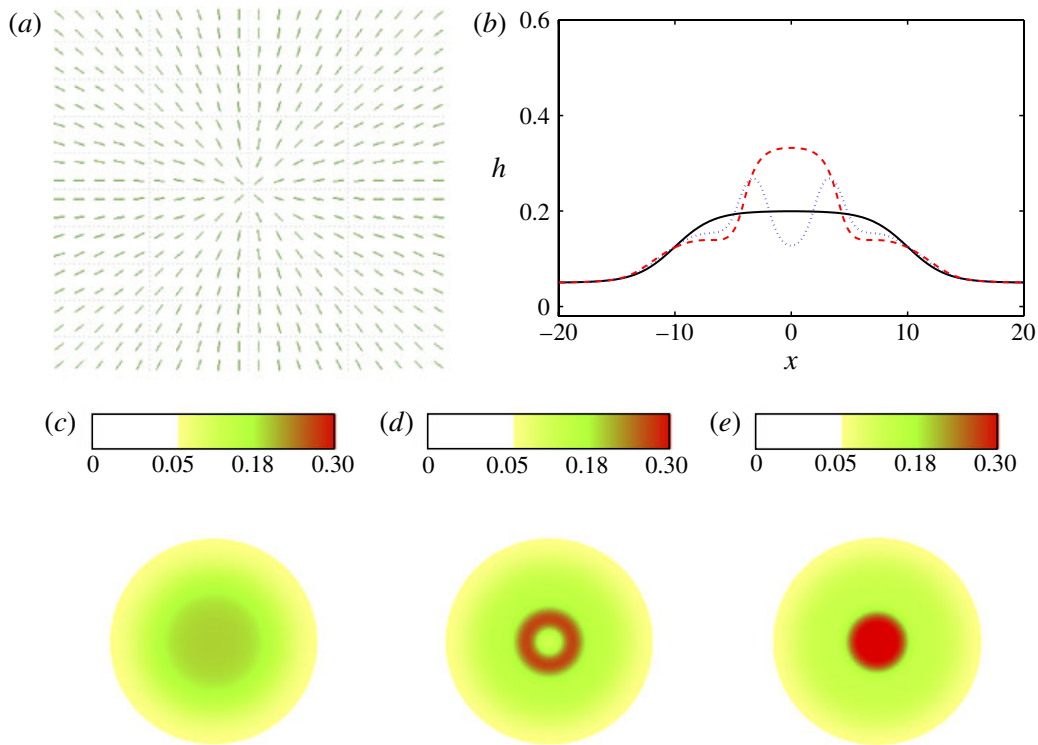

FIGURE 6. (Colour online) Spreading NLC droplet for $\mathcal{N} = 1$ and $s = 1$. The anchoring condition at the substrate is shown in (a). The cross-sections of the droplet, $h(x, y = 0, t)$, are shown in (b) for $t = 0$ (solid (black) curve), $t = 300$ (dotted (shown in blue online) curve) and $t = 600$ (dashed (shown in red online) curve). The contour of the droplet at $t = 0$, $t = 300$ and $t = 600$ are shown in (c–e), respectively.

remains circular for all time, while the surface exhibits radially symmetric instabilities, as anticipated. The instabilities appear as a ring (two humps in the cross-section), which eventually closes up into a single central hump for long times.

4. Conclusions

We have presented a new model that describes 3D spreading of thin films and droplets of NLC. To the best of the authors' knowledge this is the first model of this kind to account for the effect of director variation in three dimensions on the shape of the overlying free surface. The stripe pattern of nematic films in a 3D setting was already analysed by Lavrentovich & Pergamenshchik (1994), Sparavigna, Lavrentovich & Strigazzi (1994) and Manyuhina & Ben Amar (2013) assuming the film remains a flat film. There the predicted instability mechanisms depend on the ratio of the various elastic constants while here the presented mechanism results from the coupling of free surface modulations and director orientation as described by the one-constant approximation.

Strong anchoring boundary conditions on the director at both boundaries are not suitable to describe a very thin spreading film (the director polar angle θ becomes singular at a contact line, leading to a strong diffusion, which is always stabilizing). Instead, we impose weak conical surface anchoring on the polar angle θ, with the anchoring energy given by (2.22). The anchoring at the substrate $z = 0$ is taken to be strong and planar, with the azimuthal director angle $\phi(x, y, 0)$ specified. Our formulation preserves the property of strong anchoring when the film is thick, while allowing the director to relax to a state of planar alignment (although with anisotropy entering through non-uniform azimuthal patterning) when the film is very thin. The resulting equation for the film or droplet evolution is a fourth-order nonlinear parabolic PDE, (2.39).

A simple LSA of (2.39) in the case of purely two-dimensional flow predicts that a flat film may be unstable under certain conditions. The strong anchoring limit leads to a purely diffusive contribution from the elastic effects that always acts in a stabilizing manner; but weak anchoring can lead to instability. The physical mechanism is based on a coupling of the degrees of freedom of director orientation within the film and at its surfaces and the shape of the free surface itself. Even in the limit of instantaneous director relaxation considered here this coupling gives rise to an instability mechanism active in the film thickness range where anchoring and bulk elastic energies compete. A second mechanism that can lead to patterned spreading (which might be viewed as an instability in the advancing front) is that the anchoring condition on the azimuthal angle (ϕ) at the solid substrate affects the speed of spreading. A drop spreads faster/slower when the substrate anchoring is parallel/perpendicular to the flow. For a substrate characterized by non-uniform anchoring conditions, the fluid front advances non-uniformly, in line with the prescribed anchoring patterns. This behaviour is exemplified by the analysis of a film spreading over a substrate with a striped anchoring pattern, leading to evolution with a sawtooth pattern in the advancing front, shown in figure 1.

We carried out numerical simulations of 3D spreading droplets for a variety of substrate anchoring patterns, focusing particularly on patterns that mimic the director structure near topological defects. Our simulations (including more than are reproduced here) indicate that: (i) the flat film stability analysis serves as a remarkably good indicator of the stability of more complex spreading droplets, provided that the initial 'droplet height' is well characterized; and (ii) although substrate anchoring clearly affects spreading speed and the shape of the spreading front, it does not appear to influence the global free surface stability of spreading droplets.

Although simplified, the proposed model and the reported simulations provide valuable insight into the dynamics of spreading nematic droplets and films as observed experimentally by Poulard & Cazabat (2005), Delabre *et al.* (2009) and

Manyuhina *et al.* (2010). The model as given by (2.39) is rather general, relying only on the validity of the lubrication scaling (which in turn relies only on the droplet aspect ratio), the strong anchoring condition at the substrate and the two-point trapezium rule approximation for the integral expressions appearing in (2.36). Note that we propose and use a particular reasonable form for the anchoring function $m(h)$ only where it is necessary to carry out simulations or to demonstrate possible (in)stability regions. Thus, whenever the anchoring function $m(h)$ is obtained experimentally (as an empirical function to be fitted), equation (2.39) is applicable and its predictions for the stability of a suitably thin flat film should be valid.

However, there is still much to be done in order to elicit the full story in all of its complexity. The results presented here, in particular regarding the influence of substrate anchoring patterns, clearly represent only a small subset of the possible spreading behaviour. Only very simple spreading scenarios and anchoring conditions are studied here, and it would clearly be of interest to simulate droplets spreading over more complex substrate patterning; for example, droplets spreading over several model defects as might be relevant in physical experiments. Our suggestion that the proposed substrate anchoring patterns may be thought of as idealized representations of defects in physical flows may of course also be questioned: it is known that the continuum nematic description used here breaks down in a small (nanometre) region around any defect, so our model cannot give an accurate description within such a defect core. Nonetheless, our simulations give some useful insight as to the effect that patterned planar anchoring can have on droplet evolution, and the similarity of figure 5(*c*) to parts of figure 2(*c*) in Poulard & Cazabat (2005) is intriguing.

While qualitatively illuminating, some aspects of our model are undoubtedly overly simplistic: our contact line regularization may not adequately model the true physics as the ultra-thin precursor film is approached and molecular effects such as van der Waals' interactions become important; and indeed it may well not capture the true behaviour of the anchoring conditions. The effect of finite surface anchoring energy at the substrate may also need to be taken into consideration: the relative anchoring strengths at two bounding surfaces were found to be important in the transition behaviour of the director field (albeit in the presence of an applied electric field) by Barbero & Berberi (1983) (see also citing works). In future work we plan to introduce improved models for these aspects of the problem.

Acknowledgements

REFERENCES

BARBERO, G. & BERBERI, R. 1983 Critical thickness of a hybrid aligned nematic liquid crystal cell. *J. Phys. (Paris)* **44**, 609.

BEN AMAR, M. & CUMMINGS, L. J. 2001 Fingering instabilities in driven thin nematic films. *Phys. Fluids* **13**, 1160.

BLOSSEY, R., MÜNCH, A., RAUSCHER, M. & WAGNER, B. A. 2006 Slip vs. viscoelasticity in dewetting thin films. *Eur. Phys. J.* E **20**, 267.

CAROU, J. Q., MOTTRAM, N. J., WILSON, S. K. & DUFFY, B. R. 2007 A mathematical model for blade coating of a nematic liquid crystal. *Liq. Cryst.* **34**, 621.

CUMMINGS, L. J. 2004 Evolution of a thin film of nematic liquid crystal with anisotropic surface energy. *Eur. J. Appl. Maths* **15**, 651.

CUMMINGS, L. J., LIN, T.-S. & KONDIC, L. 2011 Modeling and simulations of the spreading and destabilization of nematic droplets. *Phys. Fluids* **23**, 043102.

DE GENNES, P. G. & PROST, J. 1995 *The Physics of Liquid Crystals*. Oxford University Press.

DELABRE, U., RICHARD, C. & CAZABAT, A. M. 2009 Thin nematic films on liquid substrates. *J. Phys. Chem.* B **13**, 3647.

LAVRENTOVICH, O. D. & PERGAMENSHCHIK, V. M. 1994 Stripe domain phase of a thin nematic film and the K13 divergence term. *Phys. Rev. Lett.* **73**, 979.

LESLIE, F. M. 1979 Theory of flow phenomena in liquid crystals. *Adv. Liq. Cryst.* **4**, 1.

LIN, T.-S., CUMMINGS, L. J., ARCHER, A. J., KONDIC, L. & THIELE, U. 2013 Note on the hydrodynamic description of thin nematic films: strong anchoring model. http://arxiv.org/abs/1301.4110.

LIN, T.-S., KONDIC, L. & CUMMINGS, L. J. 2012*a* Defect modeling in spreading nematic droplets. *Phys. Rev.* E **85**, 012702.

LIN, T.-S., KONDIC, L. & FILIPPOV, A. 2012*b* Thin films flowing down inverted substrates: three-dimensional flow. *Phys. Fluids* **24**, 022105.

MANYUHINA, O. V. & BEN AMAR, M. 2013 Thin nematic films: anchoring effects and stripe instability revisited. *Phys. Lett.* A **377**, 1003.

MANYUHINA, O. V., CAZABAT, A. M. & BEN AMAR, M. 2010 Instability patterns in ultrathin nematic films: comparison between theory and experiment. *Europhys. Lett.* **92**, 16005.

MECHKOV, S., CAZABAT, A. M. & OSHANIN, G. 2009 Post-Tanner spreading of nematic droplets. *J. Phys.: Condens. Matter* **21**, 464134.

MITLIN, V. S. 1993 Dewetting of solid surface: analogy with spinodal decomposition. *J. Colloid Interface Sci.* **156**, 491.

MÜNCH, A., WAGNER, B. A., RAUSCHER, M. & BLOSSEY, R. 2006 A thin film model for corotational Jeffreys fluids under strong slip. *Eur. Phys. J.* E **20**, 365.

MYERS, T. G. 2005 Application of non-Newtonian models to thin film flow. *Phys. Rev.* E **72**, 066302.

POULARD, C. & CAZABAT, A. M. 2005 Spontaneous spreading of nematic liquid crystals. *Langmuir* **21**, 6270.

SPARAVIGNA, A., LAVRENTOVICH, O. D. & STRIGAZZI, A. 1994 Periodic stripe domains and hybrid-alignment regime in nematic liquid crystals: threshold analysis. *Phys. Rev.* E **49**, 1344.

THIELE, U. 2010 Thin film evolution equations from (evaporating) dewetting liquid layers to epitaxial growth. *J. Phys.: Condens. Matter* **22**, 084019.

THIELE, U. 2011 Note on thin film equations for solutions and suspensions. *Eur. Phys. J. Special Topics* **197**, 213.

THIELE, U., ARCHER, A. J. & PLAPP, M. 2012 Thermodynamically consistent description of the hydrodynamics of free surfaces covered by insoluble surfactants of high concentration. *Phys. Fluids* **24**, 102107.

WITELSKI, T. P. & BOWEN, M. 2003 ADI schemes for higher-order nonlinear diffusion equations. *Appl. Numer. Maths* **45**, 331.